The 12th Swedish
Aerospace Technology Congress
F12025 in Stockholm
October 14-15, 2025

Reentry flow and aerothermal characteristics of a retro-propulsive booster

Aaron Rovelstad¹, Mohammed Kassem¹, Alexandre Capitao Patrao², Jan Östlund², Carlos Xisto¹

¹Department of Mechanics and Maritime Science, Chalmers University of Technology, Gothenburg, SE-41296, Sweden E-mail: aaronr@chalmers.se, mohkas@chalmers.se, <a href="mailto:carlos:carl

Abstract

Retro-propulsion of a rocket booster is a topic of rising interest where companies are striving to develop reusable launchers in order to reduce cost, environmental impact and turnover time. Understanding the loads on the nozzles during reentry is key to be able to design and produce nozzles capable to reliably be used multiple times. During the project a tool was developed based on CAD and flight data of a Falcon 9 based rocket. A case was set up and simulated with the help of computational fluid dynamics (CFD) and chemical models in order to understand the flow behaviour and thermal loading on and near the nozzles during two flight altitudes with- and without retro-propulsion. The results concluded that without retro-propulsion, the most exposed area, with highest heat transfer coefficient (HTC) and heat flux, are the throats of the nozzles due to a recirculation within the nozzle cluster stagnating the flow at that region. While with retro-propulsion, the thermal loads were similar in magnitude for start and end burn with local high values at the exit of the nozzles. The major thermal loads during retro-propulsion where due to expansion of the exhaust hitting the nozzle walls due to plume-plume interaction.

Keywords: Retro-propulsion, Hypersonic flow, Reentry vehicles, Computational Fluid Dynamics, Chemical modelling

1 Introduction

Retro-propulsion, a concept explored since the 1950s primarily for landing on celestial bodies, has gained renewed interest with the advent of reusable launch vehicles aimed at reducing costs and enhancing sustainability for Earth-orbit payloads [1]. Prominent private companies such as SpaceX, Blue Origin, and Rocket Lab have spearheaded this development, with SpaceX's Falcon 9 and Falcon Heavy rockets being notable examples. Despite their advancements, limited public information and validation results constrain research in this field due to the high costs associated with launches. [1]

In response, the European Space Agency (ESA) has initiated several projects under the Future Launchers Preparatory Programme (FLPP) to bolster European capabilities in reusable rocket boosters. Key projects include RETPRO [4], focusing on CFD and wind tunnel verification of aerothermal calculations, and RETALT [2], which investigates system components of reusable boosters. Additionally, the CALLISTO project, a collaboration between CNES (France),

DLR (Germany), and JAXA (Japan), is developing a demonstrator rocket to advance retro-propulsion research.

GKN Aerospace contributes to this effort through the development of the Prometheus engine [4], a liquid methane and liquid oxygen-powered gas generator cycle engine, intended for the rocket demonstrator, Themis. The rocket aims to validate the feasibility of a reusable first-stage rocket for future Ariane missions.

This study aims to simulate the reentry and retro-propulsion phases of a first-stage liquid methane-oxygen fueled rocket, with a primary focus on the reentry burn where thermal and velocity loads are most significant. The objective is to understand the interaction between the exhaust plume and the bow shock, and to evaluate the resulting thermal and pressure loads on the baseplate and nozzles. CFD simulations of an open source, Falcon 9-inspired rocket geometry are carried out for reentry conditions at two different hypersonic speeds, including engine operation.

2 Methodology

This section describes the methodology of the different cases that were carried out and dives into the rocket geometry and the phases of flight that were investigated. The meshing tools used will be described and a mesh study will be shown. Lastly the CFD model will be presented which includes the turbulence models, reaction mechanisms and boundary conditions used along with the type of CFD software. Due to the severe computational costs of the simulations, significant time was spent on a pre-study with a 2D axisymmetric rocket model with only one centre nozzle. This was done to more cost effectively investigate the effects of potential model reductions and to be able to assess the effect of different chemical models.

2.1 Cases

The different cases investigated in this study are:

- Start of the reentry burn without retro-propulsion.
- Start of the reentry burn with retro-propulsion
- End of the reentry burn without retro-propulsion.
- End of the reentry burn with retro-propulsion

The flight conditions during reentry burn were taken from a study by DLR where they developed a reference trajectory for a downrange landing of a Falcon 9 based model [3]. The flight conditions during the start and end of the reentry burn are the following:

Table 1: Farfield operating conditions during reentry burn.

	Start burn	End burn
Altitude [km]	57.66	39.07
Pressure [Pa]	30.0	327.6
Temperature [K]	253	247
Mach [-]	7.14	5.35

For all the different cases the adiabatic temperature, the heat transfer coefficient (HTC), pressure and heat flux were calculated. For the cases with retro-propulsion, an exit profile for the velocity, temperature and pressure were taken from a 2D axisymmetric simulation [4] and set/interpolated on the nozzle exit surface.

Before the main study, a pre-study was conducted in 2D in order to run multiple simulations at a lower computational cost. The goal of the pre-study was to investigate the effects of model settings and potential model reductions in order to run more accurate simulations in 3D during the main study. One of the primary objectives during the pre-study was to investigate the impacts of the chemical model on the temperature and flow behaviour.

2.2 Geometries

The rocket geometry (46 m long and 3.6 m in diameter) used in this study is based on a 3D model in a reentry configuration inspired by the Falcon 9 used and developed by DLR [3]. To ease meshing and decrease computational costs, the geometry is modified to remove components (landing gear and fins) that are not evaluated in the present study. As the focus of the study is to investigate the thermal loads and flow behaviour on and around the nozzles, the simplifications are deemed to not impact the results. The rocket is designed to exhibit symmetry as well as the flow as no inclination is included, consequently the model was divided into a quarter, decreasing the size of the computational domain while keeping geometric integrity. The DLR model and the final 3D model used in this study is shown below in Figure 1. For the pre-study in 2D, the outer nozzles were removed keeping only the centre nozzle, in order to achieve an axisymmetric design. A contour was then cut out of the rocket to capture the shape of the rocket as well as the outer contour of the nozzle.



Figure 1: Comparison between the rocket model from DLR [3] at the left and the modified model used in this study at the right.

2.3 Meshing

ANSYS Fluent Meshing was used as a meshing tool for all the 3D simulations. The generated domain was based on an unstructured polyhedral mesh with a requirement of a $y^+ < 0.1$ to ensure that the simulations are resolving both the velocity and thermal boundary layers at the nozzle walls and baseplate. A y^+ < 1 for the rest of the rocket is used. In order to decrease the model size, two meshes were used, one for the simulations with retro-propulsion and another without retropropulsion. This was possible because the simulations without retro-propulsion did not need to resolve the plume flow, making it possible to remove the mesh refinement in this specific region. The domain used was a quarter of a cylinder and is displayed below in Figure 2. For the 2D simulations, the meshing tool ANSYS ICEM CFD was used to create a structured mesh with the same y+ requirement as for 3D.

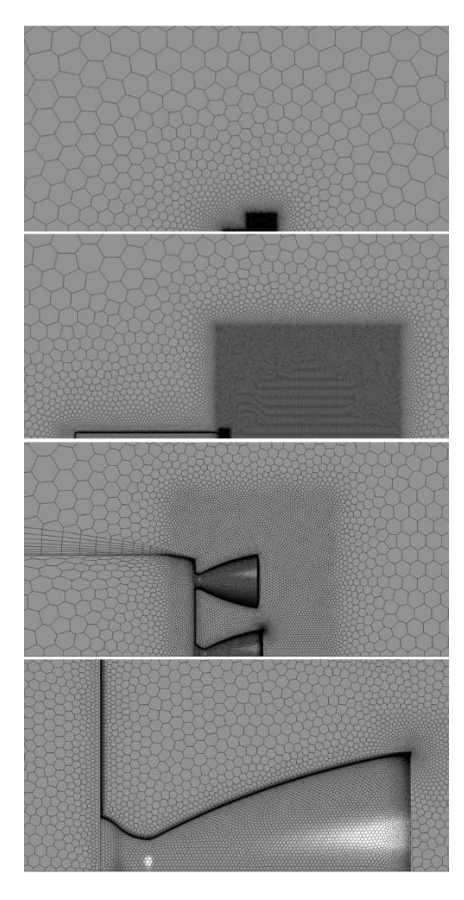


Figure 2: The volume mesh for the 3D simulation during retro-propulsion.

A mesh convergence study was done with frozen chemistry for both the 3D grids and a Richardson extrapolation was used to evaluate the level of spatial convergence. The Richardson extrapolation was implemented using the following equations:

$$p = ln \left(\frac{f_3 - f_2}{f_2 - f_1} \right) / ln(r)$$

$$f_0 \cong f_1 + \frac{f_1 - f_2}{r^p - 1}$$

$$r = \frac{h_1}{h_2}$$

Where p is the order of convergence, r is the grid refinement ratio, f_3 , f_2 and f_1 are the area-weighted average of the wall temperature for coarse, medium and fine grids respectively and h_1 and h_1 are the finer and coarser grid spacing respectively. The results for the mesh convergence study for the two grids are shown in Table 2 and Table 3. The properties in the tables (wall temperature and y^+) are taken as an area-weighted average on the centre nozzle wall. For the simulations with retro-propulsion there is a 5.54 % difference between the finest mesh and the extrapolated value, indicating that a finer mesh is required. However, it

was noted that, with the finest mesh, the initialisation of the model with a chemical non-equilibrium reaction scheme, the software required an impractical amount of RAM. This resulted in the development of a reduced chemical model (more about this in section 2.4), with which it was possible to run the finest mesh, but put a limitation in further refinement. Even though the solution requires a finer mesh, this analysis will be on the conservative side as the temperatures and heat fluxes will be higher than would be achieved for a fully mesh independent solution.

Table 2: Mesh convergence study for the 3D case with retropropulsion, fine is the chosen mesh.

Mesh	$N_{cells}[10^6]$	T [K]	Δ T [%]	y ⁺
Richardson	-	3018.9	0	-
Extrapolation				
Fine	6.24	3186.9	5.54	0.045
Medium	2.45	3249.0	7.59	0.060
Coarse	0.989	3333.4	10.41	0.074

For the second mesh without retro-propulsion, it's evident from Table 3 that the solutions are mesh independent as all the 3 meshes have a difference of less than 0.07 %. However, the medium mesh was chosen as it had good trade-off between numerical dissipation across the shock and computational efficiency. The increase in y^+ for the medium mesh is due to the transition ratio of the inflation layers that was adjusted to increase mesh quality. As the y^+ is close to the desired value of 0.1, it was considered fine enough. Due to sharp gradients near the exit of the nozzle, a refinement was made to the medium mesh to increase resolution in this specific area. This increased the number of cells and resulted in a temperature of 2458.1 K which is a 0.0244 % decrease from the chosen medium mesh and therefore acceptable to use.

Table 3: Mesh convergence study for the 3D case without retro-propulsion.

Mesh	$N_{cells}[10^6]$	T [K]	ΔT [%]	y^+
Richardson	-	2457.2	0	-
Extrapolation				
Fine	1.54	2457.6	0.043	0.089
Medium	0.63	2458.7	0.085	0.111
Coarse	0.336	2458.9	0.097	0.089

A mesh independence study was also done for the 2D grid, and it showed that the chosen resolution provided a 0.169 % difference in area-weighted average wall temperature on the centre nozzle compared to the extrapolated value.

2.4 CFD modelling

The CFD computations were performed in ANSYS Fluent 2024 R1 using a steady state RANS solver with the $k-\omega$ SST turbulence model. A near wall treatment based on a y^+ -insensitive correlation was used to model the flow near

the solid walls. The y^+ treatment uses an analytical expression to blend between the viscous and the logarithmic sublayers. For $y^+ < 5$ a low Reynolds number formulation is used and for $y^+ > 30$ wall functions will be implemented. The generated mesh was designed to ensure that a low Reynolds number formulation would be utilized across all the computations. The CFD model is implemented in an implicit density-based solver with a second order spatial discretization scheme for the pressure, momentum and energy equation but also for the turbulent kinetic energy and specific dissipation rate. The following governing equations are solved:

$$\begin{split} \frac{\partial \rho}{\partial t} + \frac{\partial \rho v_i}{\partial x_i} &= 0, \\ \frac{\partial \rho v_i}{\partial t} + \frac{\partial \rho v_i v_j}{\partial x_j} &= -\frac{\partial P}{\partial x_i} + \frac{\partial \tau_{ij}}{\partial x_j} + \rho f_i, \\ \frac{\partial \rho e_0}{\partial t} + \frac{\partial \rho e_0 v_j}{\partial x_i} &= -\frac{\partial P v_j}{\partial x_i} + \frac{\partial}{\partial x_i} \bigg[C_p \frac{\mu}{P_r} \frac{\partial T}{\partial x_i} + v_i \sigma_{ij} \bigg]. \end{split}$$

The $k - \omega$ SST turbulence model used solves the following equations:

$$\begin{split} \frac{\partial \rho k}{\partial t} + \frac{\partial \rho u_j k}{\partial x_j} &= P_k - \beta^* \rho \omega k + \frac{\partial}{\partial x_j} \bigg[(\mu + \sigma_k \mu_t) \frac{\partial k}{\partial x_j} \bigg], \\ \frac{\partial \rho \omega}{\partial t} + \frac{\partial \rho u_j \omega}{\partial x_j} &= \gamma P_\omega - \beta \rho \omega^2 + 2\rho (1 - F_1) \sigma_{\omega^2} \frac{1}{\omega} \frac{\partial k}{\partial x_j} \frac{\partial \omega}{\partial x_j} \\ &\quad + \frac{\partial}{\partial x_j} \bigg[(\mu + \sigma_\omega \mu_t) \frac{\partial \omega}{\partial x_j} \bigg]. \end{split}$$

In order to evaluate the HTC the following equation will be utilised,

$$q = h(T_{aw} - T_w),$$

where q is the computed heat flux trough the wall, h is the heat transfer coefficient, T_{aw} is the adiabatic wall temperature and T_w is the prescribed wall temperature.

As the temperature of the gas increases, different chemical phenomena happen where the thermophysical properties become non-constant or species start to react. There is also significant post combustion of the high temperature exhausts which needs to be modelled in order to achieve accurate results. However, these chemical models lead to a significant increase in computational costs, which is why the impact of the chemical models was investigated in a pre-study in a 2D model.

To be able to simulate high temperature gases, present in hypersonic flight conditions, the choice of chemical model becomes important. In the pre-study, calorically perfect gas, frozen chemistry, chemical equilibrium and chemical non-equilibrium were studied and compared. For the 3D case, frozen chemistry was used for the simulations without retro-propulsion and chemical non-equilibrium for simulations with retro-propulsion. Each species in a CFD simulation requires on additional transport equation, given by:

$$\frac{\partial \rho Y_k}{\partial t} + \frac{\partial \rho u_i Y_k}{\partial x_i} = \frac{\partial}{\partial x_i} \left(\rho D_k \frac{\partial Y_k}{\partial x_i} \right) + \omega_k.$$

Where Y_k is the species k, D_k is the diffusion coefficient for the species and ω_k is the source term used to model the chemical reactions. For the assumption of frozen chemistry, the source term will be zero because the model does not allow for any reactions to take place; i.e. only the transport and diffusion of species is considered. For a reacting flow the source term will depend on the production and destruction of the given species. This source term is calculated as

$$\omega_k = M_i \sum_{r=1}^{N_r} (\nu_{kr}^{"} - \nu_{kr}^{"}) \left[k_{fr} \prod_{j=1}^{N_s} \left(\frac{\rho_j}{M_j} \right) \nu_{jr}^{"} - k_{br} \prod_{j=1}^{N_s} \left(\frac{\rho_j}{M_j} \right) \nu_{jr}^{"} \right].$$

Where M_i is the molecular weight, N_r is the total number of reactions of species i, v_{kr} is the stoichiometric coefficient of species k in reaction r, while k_{fr} and k_{br} are the forward and backward rate of reaction coefficients. The forward and backward rate coefficients, k_{fr} and k_{br} , are calculated with the semi-empirical equation modified Arrhenius equation, defined as

$$k_{fr} = A_r T^n e^{\frac{-E_r}{RT}},$$

where A_r is pre-exponential factor, n is the exponent making the pre-exponent temperature dependent, E_r is the activation energy, T is the temperature and R is the universal gas constant. The constants A_r , n and E_r are derived from experimental data and will vary depending on the chosen chemical reaction The scheme. transport thermodynamical properties used in the simulations are taken from CHEMKIN transport- and thermodynamical databases. The reduced air-reaction model, proposed by Park2001 [5] is used for solving the Arrhenius equations fohypersonic flow in reentry vehicles. Combustion is modelled using the Zhukov-Kong [6] reduced reaction scheme for methane-LOx mixtures that was developed for liquid rocket engines. For simulations without retro-propulsion, only the Park2001 scheme was used, and for simulations with retro-propulsion the Park2001 scheme was used together with the Zhukov-Kong model.

Park2001 is a reduced 5-species air model containing N_2 , O_2 , NO, O and N [5]. The air was modelled as a composition with mass fractions of 24 % O₂ and 76 % N₂, values taken from [7]. The reaction scheme for the engine exhaust differed during this study. During the pre-study, the Zhukov-Kong's 23 species scheme, reduced from their larger 207 species scheme [6], was used. The modification of removing Argon and Helium was made to the scheme to reduce its size as there would have been a negligible amount in the flow. The final combined scheme resulted in a 24 species scheme and was used for the 2D pre-study case. As mentioned in 2.3 the 24 species model resulted in high RAM requirement for the 3D case which lead to the development of a reduced 13 species model where only the species with a mass fraction of over 10^{-7} was kept. The species, reactions and reaction parameters of the resulting methane combustion model are displayed in Figure 3. The reduced 13 specie model

was compared to the original 24 species during the pre-study in 2D, which showed a near perfect correlation in flow temperature and shockwave placement. This means that the reduced model was able to capture all of the relevant reactions in the flow that the original chemical model was able to capture. All 3D simulations with the engines on utilized the reduced 13 species model.

	Species				
	$H_2, H, O, O_2, OH, H_2O, HO_2, H_2O_2, CO, CO_2$				
	Reaction	, 2 , 2,	2 2/		Note
		A_r	n	E_r	Note *
2.	$H + O_2 + M \leftrightarrow HO_2 + M$	$2.800 \cdot 10^{18}$	-0.860	0.000	*
3.	$H + 2O_2 \leftrightarrow HO_2 + O_2$	$3.000 \cdot 10^{20}$	-1.720	0.000	
5.	$2OH(+M) \leftrightarrow H_2O_2(+M)$	$7.400 \cdot 10^{13}$	-0.370	0.000	*
6.	$OH + HO_2 \leftrightarrow O_2 + H_2O$	$2.900 \cdot 10^{13}$	0.000	-500.000	
7.	$OH + H_2O_2 \leftrightarrow HO_2 + H_2O$	$1.750 \cdot 10^{12}$	0.000	320.000	Duplicate
8.	$OH + H_2O_2 \leftrightarrow HO_2 + H_2O$	$5.800 \cdot 10^{14}$	0.000	$9.560 \cdot 10^{3}$	Duplicate
10.	$2HO_2 \leftrightarrow O_2 + H_2O_2$	$1.300 \cdot 10^{11}$	0.000	$-1.630 \cdot 10^3$	Duplicate
11.	$2HO_2 \leftrightarrow O_2 + H_2O_2$	$4.200 \cdot 10^{14}$	0.000	$1.200 \cdot 10^4$	Duplicate
14.	$HO_2 + CO \leftrightarrow OH + CO_2$	$1.500 \cdot 10^{14}$	0.000	$2.360 \cdot 10^{4}$	
26.	$H + O_2 \leftrightarrow O + OH$	$8.300 \cdot 10^{13}$	0.000	$1.4413 \cdot 10^4$	
27.	$H + O_2 + H_2O \leftrightarrow HO_2 + H_2O$	$9.380 \cdot 10^{18}$	-0.760	0.000	
28.	$O + H_2 \leftrightarrow H + OH$	$5.000 \cdot 10^4$	2.670	$6.290 \cdot 10^{3}$	
30.	$O + CO + M \leftrightarrow CO_2 + M$	$6.020 \cdot 10^{14}$	0.000	$3.000 \cdot 10^3$	*
31.	$H + OH + M \leftrightarrow H_2O + M$	$2.200 \cdot 10^{22}$	-2.000	0.000	*
37.	$OH + H_2 \leftrightarrow H + H_2O$	$2.160 \cdot 10^{8}$	1.510	$3.430 \cdot 10^{3}$	
44.	$O_2 + CO \leftrightarrow O + CO_2$	$2.500 \cdot 10^{12}$	0.000	$4.7800 \cdot 10^4$	
45.	$OH + CO \leftrightarrow H + CO_2$	$4.760 \cdot 10^{7}$	1.228	70.000	
50.	$H + O_2 + N_2 \leftrightarrow HO_2 + N_2$	$2.600 \cdot 10^{19}$	-1.240	0.000	

Figure 3: Reduced methane combustion model, combined with Park2001 [5] to make the 13-species model. Constants from Arrhenius equation, preexponential factor A_r in [cal/mole] and activation energy E_r in [mole-cm-s-K].

The following boundary conditions was used in the 3D simulations:

- **Pressure far-field:** A pressure far-field was used for the inlet, outlet and arc of the domain. The input parameters were Mach number, temperature, pressure and the chemical composition of air.
- Symmetry: A symmetry boundary condition was used for the two symmetry surfaces at each side of the quarter domain.
- Rocket walls: An adiabatic, no-slip condition was used as a boundary condition for all the rocket walls except for when the HTC was calculated. In that case the adiabatic temperature profile from the adiabatic simulation was used as a temperature boundary condition for the nozzles and rocket base plate.
- Nozzle exit: For when the engines are on, a velocity inlet is used as a boundary condition. A velocity, temperature and pressure profile from [4] is used. The mass fraction for the different species for the exhaust at the nozzle exit was taken from a NASA CEA calculation of a chemical equilibrium combustion of Methane and Oxygen. The mass fractions are presented below in Table 4. When the engines are off the same boundary condition as for Rocket walls was prescribed.

Table 4: Mass fraction of the species at the nozzle exit from NASA CEA where species with a mass fraction $< 5 * 10^{-6}$ was disregarded.

Species	Mass fraction
H ₂ O	0.45582
CO ₂	0.40774
СО	0.12849
H ₂	0.00460
ОН	0.00268
0_{2}	0.00053
Н	0.00008
0	0.00006

3 Results

The result section will go through the effects of different chemical models in 2D and determine what models to use in the 3D simulations. The HTC, heat fluxes, pressures and temperatures will be presented for the 3D simulations with and without retro-propulsion, during the start and end of the burn.

3.1 2D pre-study

In order to compare the effect of the chemical models, a data extractions line was established for the pre-study simulations, the location of which is shown Figure 4. The placement of the line was identical for simulations with and without retropropulsion, with the difference being the length of the measurement line. The location

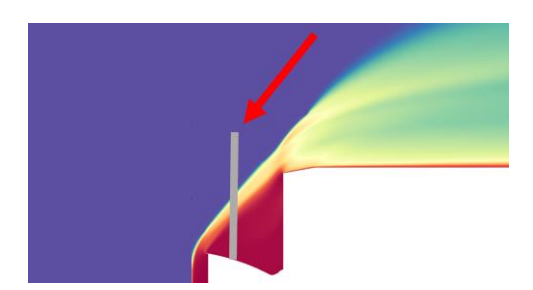


Figure 4: Data extraction line for comparison of chemical models in 2D.

It is evident, from Figure 5, that for simulations without retropropulsion, the calorically perfect gas overestimates the temperature. While frozen chemistry and chemical nonequilibrium show similar results and chemical equilibrium underestimates the temperature compared to frozen and nonequilibrium. The similar temperature from non-equilibrium and frozen chemistry is likely due to the large chemical timescales compared to flow timescales resulting in the species traveling far downstream before having sufficient time to react. The timescales and flow behaviour are not taken into consideration in the chemical equilibrium model, resulting in an overestimation in chemical activity and making the equilibrium model a less suitable model. Due to the close resemblance in temperature and shockwave placement between frozen chemistry and chemical nonequilibrium and the large computational savings, frozen chemistry was deemed an appropriate model for simulations without retro-propulsion.

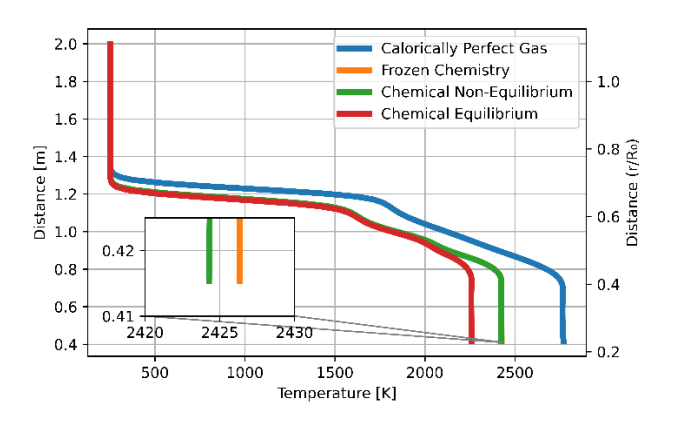


Figure 5: Comparison of temperature for different chemical models without retro-propulsion. Measured on the outer wall of the nozzle going straight up in the radial direction of the flow. The y-coordinate of the nozzle wall is at 0.4 m.

Regarding the retro-propulsion simulations, a larger spread between the models was noted in Figure 6, suggesting the presence of significant chemical reactions within the flow. The temperatures are shown to be high enough for dissociation to occur in the atmosphere as well as around the plume of the exhaust (dissociation and post-combustion). This indicates that the calorically perfect gas, as well as frozen chemistry assumptions are not appropriate models. The chemical behaviour is expected to be most accurately captured by chemical non-equilibrium, which was the chosen chemical model for 3D simulations with retro-propulsion.

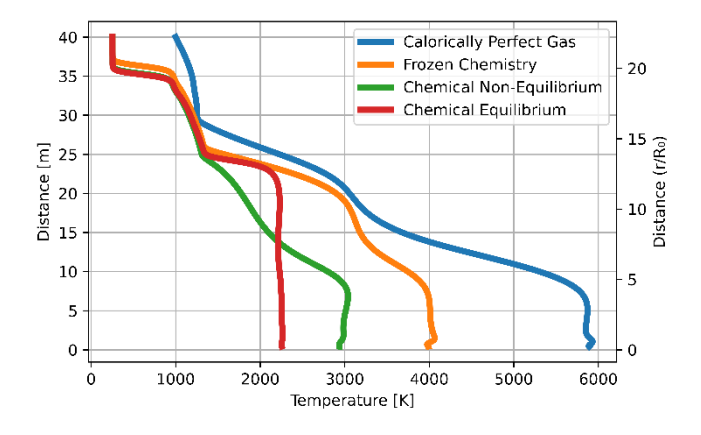


Figure 6: Comparison of temperature for different chemical models with retro-propulsion. Measured on the outer wall of the nozzle going straight up in the radial direction of the flow.

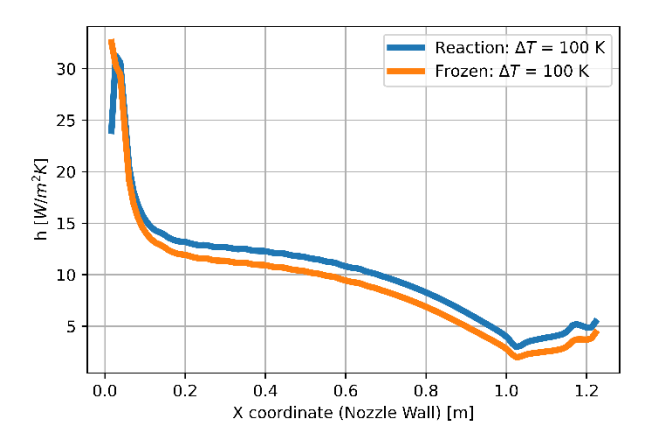


Figure 7: Comparison of HTC for frozen chemistry and reacting chemical model with retro-propulsion. Measured along the outer wall of the nozzle where x = 0 is the nozzle exit and x = 1.23 is the base of the nozzle.

A deviation in HTC on the nozzle wall was recognized when comparing frozen and reacting (chemical non-equilibrium) chemistry. As illustrated in Figure 7, reacting chemistry is expected to show slightly more conservative values, showing around 2 W/(m²K) higher HTC than frozen chemistry on average across the nozzle length. Near the exit of the nozzle, where the highest HTC is observed, the chemical models show a close resemblance, suggesting that the frozen chemistry approach assumption is a reasonable approximation due to the substantial computational savings

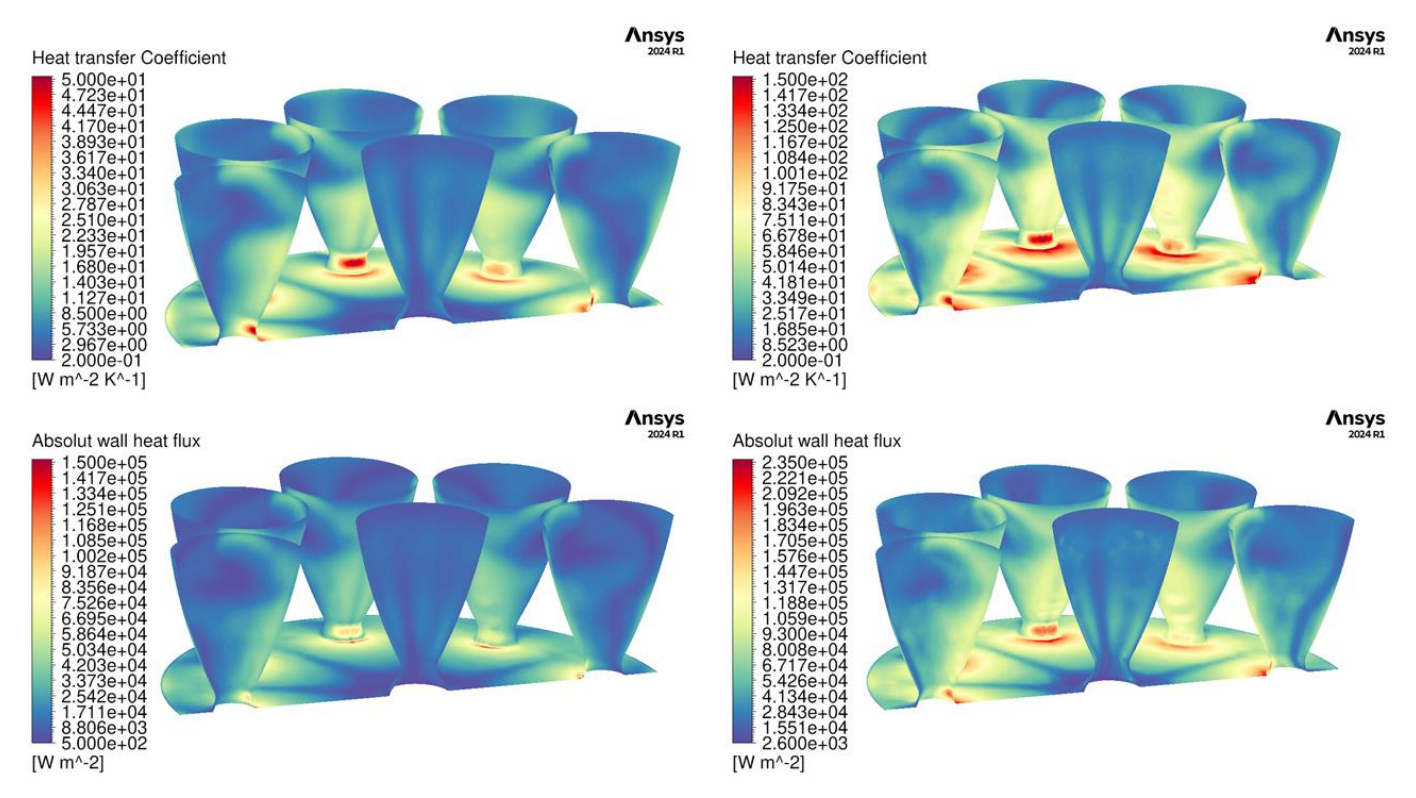


Figure 9: The HTC calculated with a $\Delta T = 100$ K and heat flux calculated with a constant $T_w = 300$ K. The left figures are at the start of the burn while the right figures are at the end of the burn.

3.2 3D simulations without retro-propulsion

The adiabatic temperature and pressure without retropropulsion is seen in Figure 8. The behavior between the two altitudes is similar but it's noted that the temperature is around a 1000 K higher at the start burn compared to the end

burn. The temperature variation is not large in either case with a fairly constant value at the center nozzle. The highest temperature for both altitudes is located near the throat and root of the nozzle. It is achieved at the same location as the highest pressure. When comparing the end burn and start burn

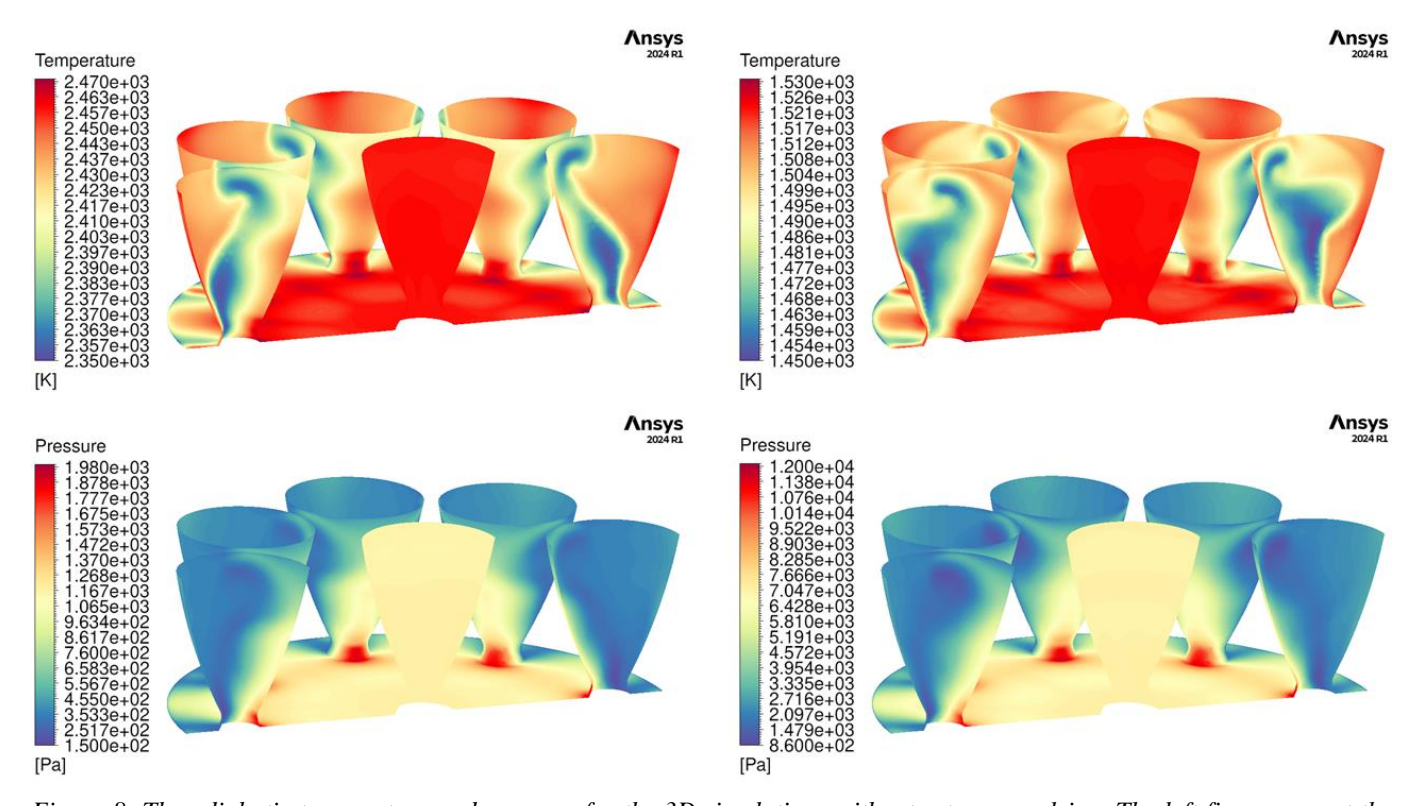


Figure 8: The adiabatic temperature and pressure for the 3D simulations without retro-propulsion. The left figures are at the start of the burn while the right figures are at the end of the burn.

the pressure is around 6 times larger at the end burn which is due to the higher atmospheric pressure at lower altitude.

A significant difference in HTC and heat flux is observed, seen in Figure 9, where values of 50 W/(m²K) and 150 kW/m² for HTC and heat flux respectively were noted for start burn while they were over 150 W/(m²K) and 230 kW/m² for end burn. The three times higher HTC during end burn is likely attributed to the higher pressures and density while the comparatively modest 50% rise of heat flux at the end burn can reasonably be associated with the lower temperature. It is evident that the highest thermal loads of the nozzle during reentry, in the absence of retro-propulsion, occurs near the throat of the nozzle and the adjacent areas on the base plate.

The flow behaviour is illustrated in Figure 11, and can assist with the explanation of the localized high values of the HTC and heat flux. The temperature is seen to significantly increase over the shockwave before flowing in between the nozzles. A recirculation area is evident between the outer nozzles and central nozzle where a stagnation point is located at the throat of the outer nozzles, in the same location as the increased HTC is found. This stagnation point is also evident in Figure 8, where elevated static pressures can be seen.

3.3 3D simulations with retro-propulsion

The plume structure, seen in Figure 10, shows significantly different behaviour depending on what plane is viewed. A larger plume is formed in the XY-plane as the exhaust can freely expand past the outer nozzles. For the XZ-plane, however, the plume-plume interaction generates shock waves constraining the expansion resulting in a more compact plume with higher Mach numbers. As shown in Figure 10 the most significant temperature increase originates from the Mach disk in the exhaust. This heat is then transported along the plume, warming the area surrounding the nozzle as well as the rocket walls. In order to increase visibility, all of the following images will be cut along the XZ-plane, in other words through all the active nozzles.

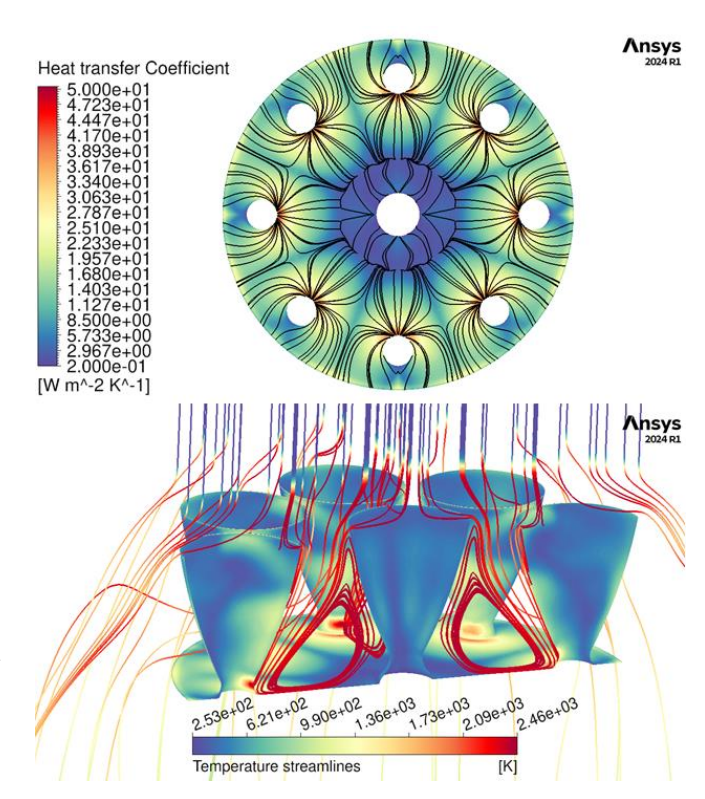


Figure 11: The HTC and the temperature streamlines at the start of the burn without retro-propulsion.

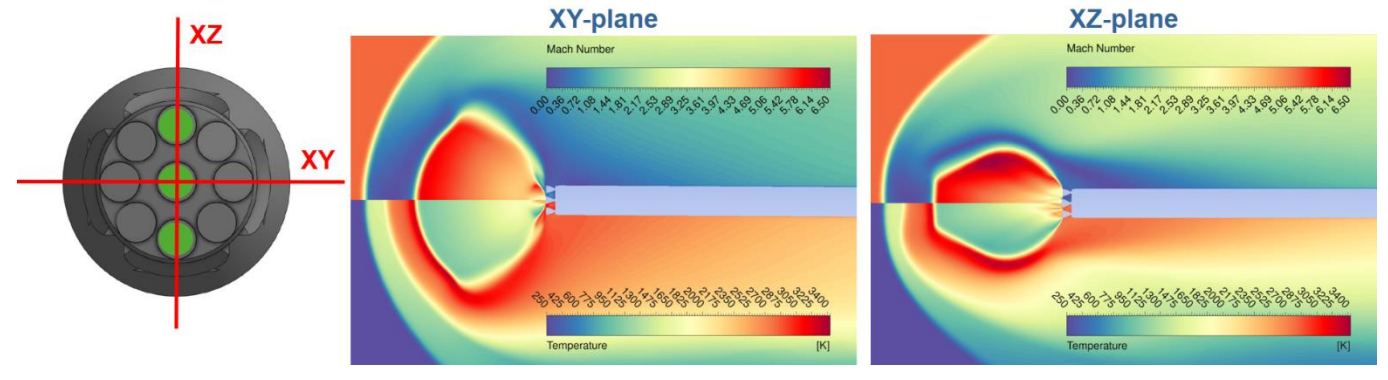


Figure 10: Plume structure from the same simulation, showing two different cutting planes for reentry with retro-propulsion. The simulation was conducted in 3D with a chemical non-equilibrium model during the end of the burn.

The adiabatic wall temperature, simulated with chemical non-equilibrium, can be seen in Figure 12. The temperatures vary between 2700 K and 3400 K where the start of the burn display a slightly higher average temperature. For start burn, higher temperatures can be seen on the outer nozzles at the sides facing the center nozzle while lower temperatures are found on the sides facing outward on the outer nozzles as well as top regions on the center nozzle. End burn has a more uniform temperature with warmer areas located on the non-active side nozzles especially the sides facing each other and the center nozzle. While the sides facing outward similarly to the start burn exhibits lower temperatures.

The adiabatic wall temperatures, simulated with frozen chemistry, used for HTC calculations are illustrated in Figure 14. These adiabatic temperatures are significantly higher than those obtained with the chemical non-equilibrium simulations and should, therefore, only be regarded as a simulation used to get the adiabatic temperature to calculate the HTC. The frozen chemistry was used as it provided similar results for HTC calculations while significantly reducing computational costs. The HTC during retropropulsion is seen in Figure 14. In contrast to the HTC without retro-propulsion, there is less of a difference between the start and end of the burn. This is due to the HTC being dependent on the exhaust from the nozzles which has the same prescribed values at the boundaries and will therefore have similar values when expanding into the nozzles. The maximum values for both simulations are approximately $150 W/(m^2 K)$ found at the edge of the nozzles close to the exit. The high values at the center nozzle have been found to be due to the exhaust from the side nozzles expanding into

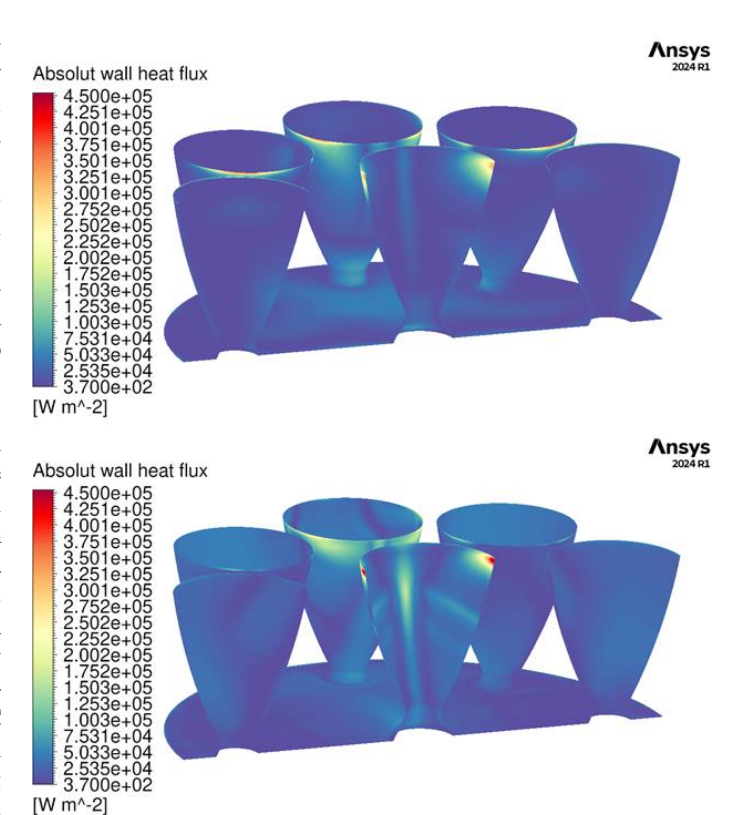


Figure 13: The heat flux calculated with T_w =300 K for the 3D simulations during retro-propulsion. The top figure is the start of the burn while the bottom figure is the end of the burn.

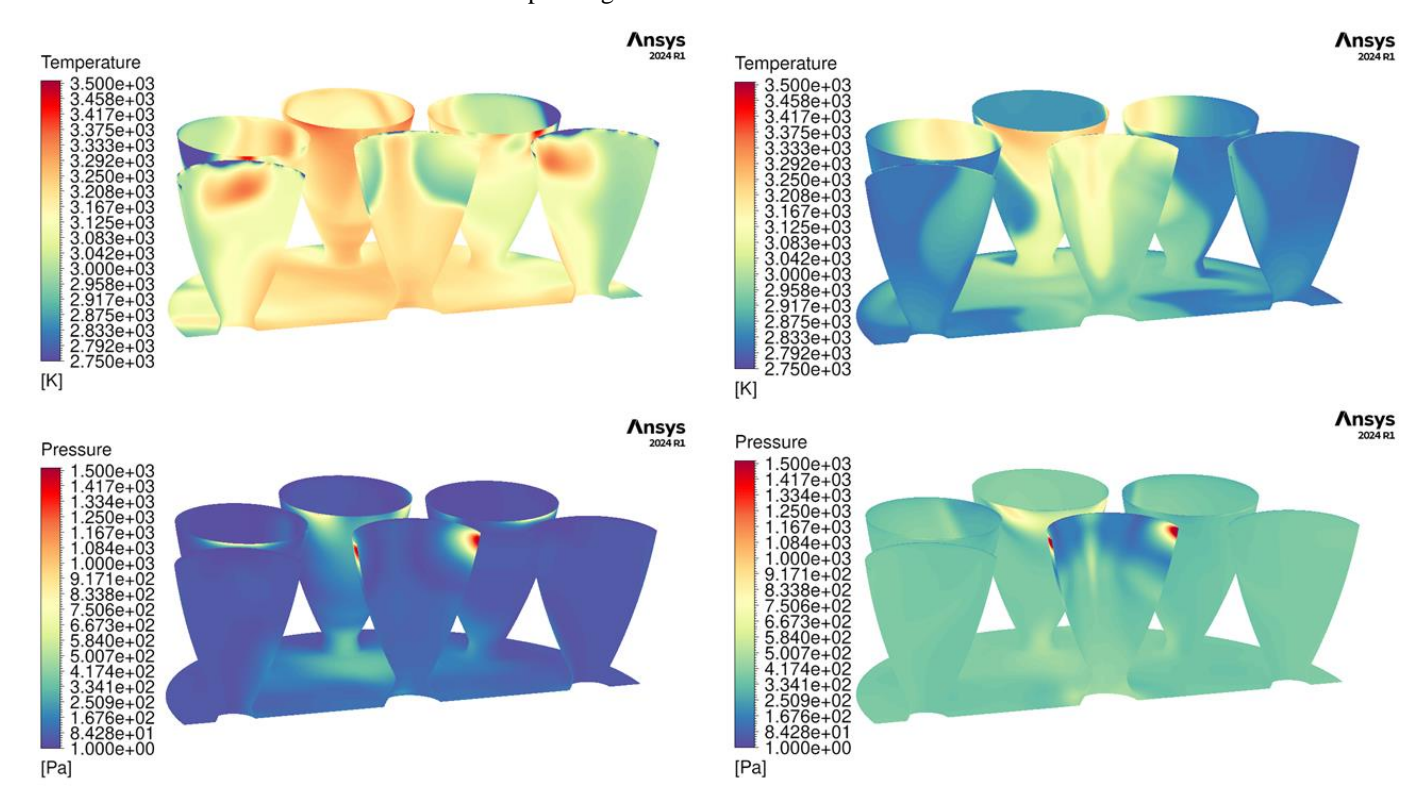


Figure 12: Adiabatic wall temperature for and pressure for the 3D simulations during retro-propulsion with chemical non-equilibrium. Left figures is start burn, and right figures is end burn.

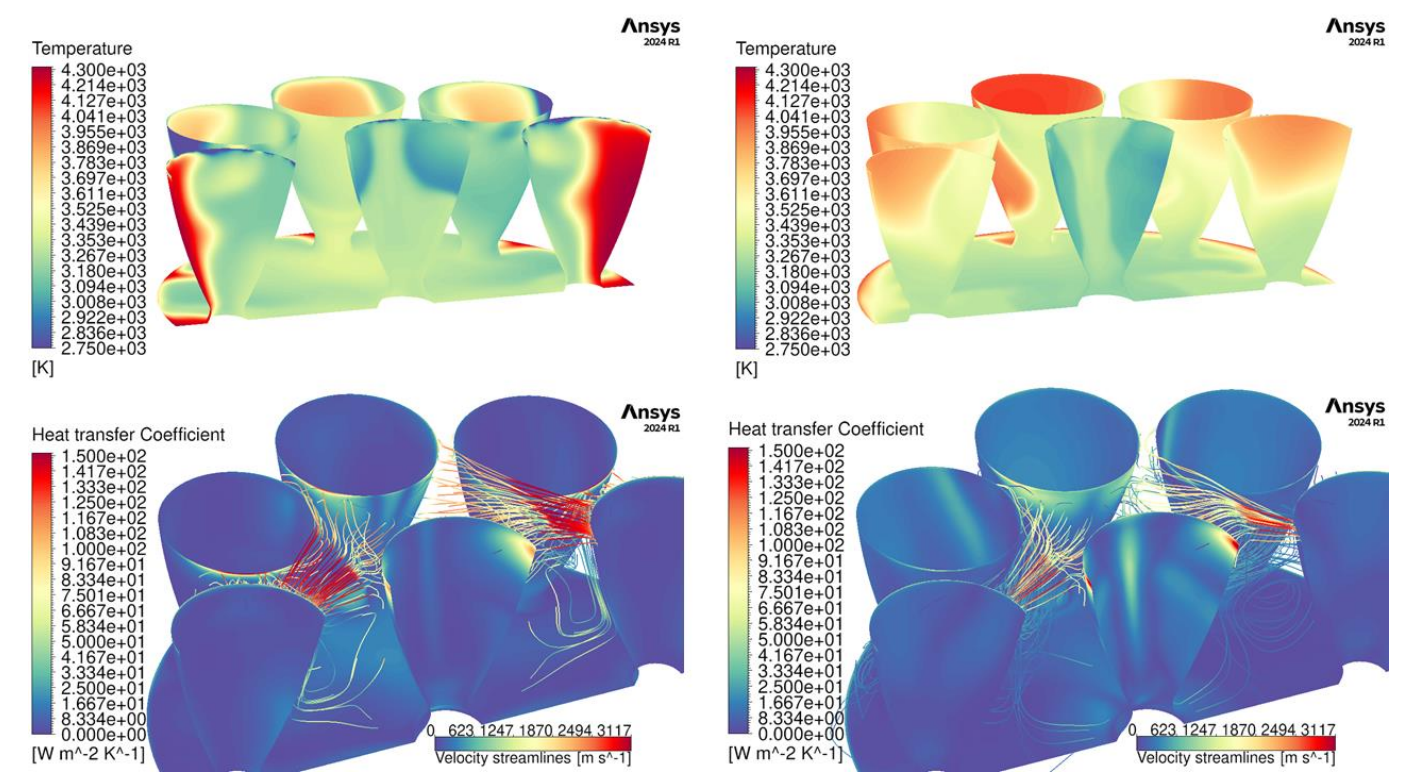


Figure 14: The HTC and velocity streamlines from the side nozzles at the bottom figures calculated with a ΔT =100 K with the frozen chemistry model during retro-propulsion. The corresponding adiabatic temperatures from the frozen chemistry model is shown in the figures at the top. The left figures are the start of the burn while the right figures are the end of the burn.

the center nozzle causing an elevated HTC. For the start of the burn the expansion is larger resulting in the exhaust expanding into the center nozzle, as well as the other outer nozzles creating local regions of high HTC. For end burn however, the higher atmospheric pressure results in a less severe expansion and therefore the majority of the flow only affects the center nozzle. The exhaust from side nozzles expanding into the center nozzle is found to be due to plumeplume interaction. As the center nozzle is slightly more extended upwards than the outer nozzles, i.e. the exit is slightly further away from the baseplate, the plume-plume interaction creates a stagnation point forcing some of the flow from the side nozzles down onto the center nozzle and into the nozzle cluster. Despite the high adiabatic temperatures on the outer nozzles facing outward, there is a negligible HTC, most likely due to the flow at that location having relatively low pressures and velocity.

The heat flux, seen in Figure 13, shows local high values in the same locations as the HTC. For start burn the values are shown to be approximately 0.4 MW/m^2 while slightly larger values of almost 0.5 MW/m^2 are found for end burn. For the start of the burn these highest values are mostly located at the edges of the outer nozzles with a region on the center also exhibiting elevated values. While at the end of the burn it's the other way around, the heat flux are higher at the exposed region on the center nozzle. This follows the behaviour shown in Figure 14. Apart from those regions both the altitudes exhibit fairly low heat fluxes.

As earlier described, the adiabatic wall temperatures are higher on the walls facing outward compared to inward. This can be explained by looking at the exhaust streamlines passing through the plume at Figure 15. The exhaust expands after exiting the nozzle up until the shockwave where the temperature drastically increases, flows backward entering a recirculation zone before flowing past and effectively cooling the outsides of the nozzles. A large temperature variation can be noted going from the shock wave into the recirculation zone. The decrease in temperature is due to endothermic reactions having sufficient time to react acting like a heat sink. This hypothesis is strengthened by the major differences between the adiabatic wall temperatures of frozen chemistry and chemical non-equilibrium (Figure 12 and Figure 14). As the frozen chemistry does not allow for any reactions, the temperatures are nearly constant flowing from the shock wave and recirculating past the nozzles. As the temperature after the shockwave for frozen chemistry is estimated to be over 4000 K, this high temperature flow recirculates and heats the outside of the nozzles causing significantly higher outer temperatures compared to chemical non-equilibrium. The temperature of the center nozzle and the nozzles facing the center nozzle are quite similar for both frozen chemistry and chemical non-equilibrium. This is due to the temperature being affected by the exhaust coming directly from the side nozzles which is flowing very fast. This is due to the temperature being affected by the exhaust coming directly from the side nozzles which is flowing very fast.

The high speeds of the exhaust prevents the species from having sufficient time to react resulting chemical nonequilibrium having a similar behaviour and temperature as frozen chemistry.

Lastly, evidence of numerical issues can be observed at the edge of the active nozzles near the exit, especially notable on the active side nozzle found on the left nozzle in the bottom figure of Figure 15. This is likely to be due to extremely low pressures, below 1 Pa, due to low ambient pressures being further reduced by the rapid expansion of the exhaust. This is further validated by the lack of numerical issues at end burn where the ambient pressures are significantly higher. These numerical issues indicate that the flight operation of start burn is close to the limit to what can be simulated using this CFD model. One way to overcome this issue could be to run the simulations fully unsteady, using a global time-step that encompasses all the resolved time-scales.

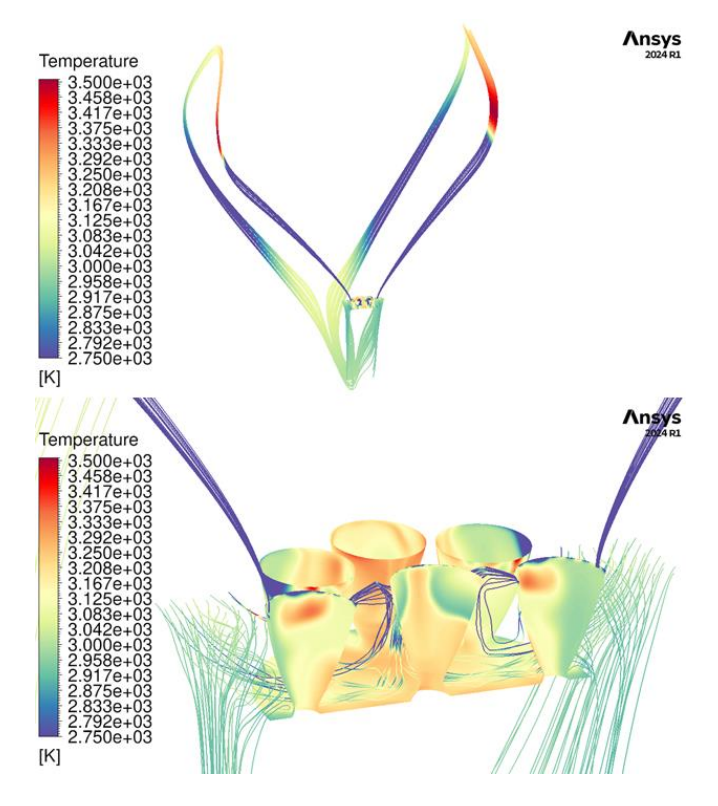


Figure 15: The adiabatic temperature and the temperature streamlines from the side nozzles at the start of the burn during retro-propulsion.

4 Conclusion

In summary, the pre-study concluded that a frozen chemistry model is an appropriate model for use without retro-propulsion and can be used when calculating HTC with retro-propulsion with only a small deviation to the chemical non-equilibrium model. However, for temperature and heat flux simulations with retro-propulsion, a chemical non-equilibrium is necessary. The pressures for both flight conditions at start and end burn are low with the highest values found at the end burn. The adiabatic wall temperatures without retro-propulsion showed that there are nearly a 1000

K higher values found at start burn with the highest value being around 2500 K. Despite the higher temperature at the start burn, the HTC and heat transfer are significantly higher during the end burn with the most exposed areas being near the throat of the nozzle. This is believed to be due to the higher pressures and density at that location. During retropropulsion, many of the local high values such as pressure, HTC and heat flux, are due to the exhaust from the outer nozzles expanding into the center nozzle wall and the other outer nozzles resulting in localised high values near the edges of the nozzles which was evident in . As the exhaust was the main cause of the significant loads, the variation between start and end burn was less compared to without retro-propulsion. The recirculation inside the engine cluster was found to be due to expansion and plume-plume interaction between the center and outer nozzles.

5 References

- [1] H. Jones, "The recent large reduction in space launch cost," 48th International Conference on Environmental Systems, 2018.
- [2] Ansgar Marwege, Josef Klevanski, Johannes Riehmer, "DELIVERABLE D 2.1, System definition report," 2019.
- [3] T. Bykerk, "A standard model for the investigation of aerodynamic and," in *Aerospace Europe Conference* 2023-10th EUCASS-9th CEAS, Lausanne, Switzerland, 2023.
- [4] Sebastian Karl, Tamas Bykerk, and Mariasole Laureti, "Design of a truncated ideal nozzle for a re-usable first stage launcher," in *HiSST: 3rd International Conference on High Speed Vehicle Science and Technology*, Busan, Korea, 2024.
- [5] Chul Park, Richard Jaffe and Harry Partridge, "Chemical-Kinetic Parameters of Hyperbolic Earth Entry," *Journal of Thermophysics and Heat Transfer J THERMOPHYS HEAT TRANSFER*, vol. 15, 2001.
- [6] Viktor P.Zhukov and Alan F.Kong, "A Compact Reaction Mechanism of Methane Oxidation at High Pressures," *Progress in Reaction Kinetics and Mechanism*, vol. 43, 2018.
- [7] D. Kirchheck, A. Marwege, J. Klevanski, J. Riehmer, A. Gulhan, S. Karl, O. Gloth, "Validation of Wind Tunnel Test and CFD Techniques for Retro-propulsion (RETPRO): Overview on a Project within the Future Launchers Preparatory Programme (FLPP)," 2019.